Skyrmion motion in synthetic antiferromagnets and ferrimagnets driven by asymmetric spin wave emission

Christopher E. A. Barker, Charles Parton-Barr, Christopher H. Marrows, Olga Kazakova, and Craig Barton, and Craig Barton, ¹National Physical Laboratory, Hampton Road, Teddington, TW11 0LW, United Kingdom ²School of Physics and Astronomy, University of Leeds, Leeds, LS2 9JT, United Kingdom ³Department of Electrical and Electronic Engineering, University of Manchester, Manchester, M13 9PL, United Kingdom

(Received 17 February 2025; revised 5 August 2025; accepted 12 August 2025; published 25 September 2025)

Skyrmions have been proposed as new information carriers in racetrack memory devices. To realize such devices, a small size, high speed of propagation, and minimal skyrmion Hall angle are required. Synthetic antiferromagnets (SAFs) present the ideal materials systems to realize these aims. In this work, we use micromagnetic simulations to propose a new method for manipulating them using exclusively global magnetic fields. An out-of-plane microwave field induces oscillations in the skyrmion radius, which in turn emits spin waves. When a static in-plane field is added, this breaks the symmetry of the skyrmions and causes asymmetric spin wave emission. This in turn drives the motion of the skyrmions, with the fastest velocities observed at the frequency of the intrinsic out-of-phase breathing mode of the pair of skyrmions. This behavior is investigated over a range of experimentally realistic antiferromagnetic interlayer exchange coupling strengths, and the results are compared to previous works. Through this we demonstrate the true effect of varying the exchange coupling strength and gain greater insight into the mechanism of skyrmion motion. In an attempt to more accurately reproduce experimental SAF samples, we investigate the effect of changing the ratio between the layer magnetizations in the SAF, and demonstrate that maximum velocity can be achieved when there is 100% compensation. We also investigate the differences between excitation mechanisms, using both electric fields and spin transfer torques to excite skyrmion motion. These results will help to inform the design of future novel computing architectures based on the dynamics of skyrmions in synthetic antiferromagnets.

DOI: 10.1103/j6y9-dj7f

I. INTRODUCTION

Magnetic skyrmions—a type of topological spin texture stabilized by the Dzyaloshinksii-Moriya interaction [1-3] are an area of great recent interest for their potential applications in magnetic memory [4,5], future computation [6,7] and quantum operations [8,9]. In all of these applications, the ability to controllably move and manipulate skyrmions is key. They can be moved with electrical currents [10-12], magnetic field gradients [13,14], and microwave magnetic fields [15,16] among other methods. However, in ferromagnetic systems, skyrmions exhibit the skyrmion Hall effect—where they travel at an angle to the driving force [17]—the magnitude of which depends on the velocity, skyrmion size and local pinning landscape [12,18-20]. This is a significant roadblock to the implementation of skyrmion based devices as skyrmions will tend to drift to the edges of devices and annihilate [21].

Published by the American Physical Society under the terms of the Creative Commons Attribution 4.0 International license. Further distribution of this work must maintain attribution to the author(s) and the published article's title, journal citation, and DOI.

Synthetic antiferromagnets—where two individually ferromagnetic layers are sandwiched around a nonmagnetic spacer layer and coupled antiferromagnetically [22]—have been predicted to be an advantageous platform for skyrmions [21,23]. This is because of their proposed smaller size, faster velocity, and increased resistance to stray fields compared to skyrmions observed in ferromagnetic systems [24]. Skyrmions with radii as small as ~50 nm have been experimentally observed in synthetic antiferromagnets [25,26]. Skyrmions and domain walls have been shown to move at substantially faster velocities than their ferromagnetic equivalents of up to 900 m/s [27] in the case of skyrmions, or 750 m/s in the case of domain walls [28]. Domain walls have also been shown to depin at current densities as low as $1 \times 10^{11} \text{ A/m}^2$ [29,30]. Due to the challenges in detection, much of the body of research on skyrmions in synthetic antiferromagnets remains theoretical [31], and experimental measurements of skyrmion motion are extremely limited [26,27,32].

Skyrmions have been shown to exhibit microwave resonances when excited by magnetic and electric fields [33]. This was originally predicted based on numerical modeling of skyrmions in bulk systems [34], and was first demonstrated experimentally in Cu₂OSeO₃ [35]. The breathing modes of skyrmions were first simulated in thin films by Kim et al. [36], and have recently been demonstrated experimentally in ferromagnetic thin films [37,38]. In synthetic antiferromagnets, micromagnetic simulations have been used to

^{*}Contact author: christopher.barker@npl.co.uk

[†]Contact author: c.h.marrows@leeds.ac.uk

[‡]Contact author: craig.barton@npl.co.uk

demonstrate both the breathing modes [39,40] and corresponding rotational modes [41]. The breathing and rotational modes of skyrmions have generated interest for magnonics, where, by exciting at the resonant frequency of these modes, they have been used as spin wave emitters [42–44]. Building on this, by exciting these breathing modes in the presence of an in-plane magnetic field, it has been demonstrated that skyrmions in ferromagnetic systems will emit spin waves asymmetrically. This stimulates skyrmion motion with a peak in velocity as a function of frequency that is coupled to the breathing mode resonant frequency [16,45]. In the presence of the in-plane field, there will be a net momentum transfer from the skyrmion to the spin waves, which will cause the skyrmion to move through the conservation of linear momentum [45,46]. This has also been demonstrated in synthetic antiferromagnets where microwave electric fields were used to excite straight-line skyrmion motion [47]. In that work, a dependence of the velocity on the strength of the antiferromagnetic interlayer exchange coupling was demonstrated, however the link between this and the skyrmion breathing modes was not discussed [47]. This microwave field driven approach to skyrmion motion has the advantage that—unlike the conventional method of using an electric current—it does not require a conductive sample, and so can be used to manipulate skyrmions in insulating materials.

In this work, we use microwave magnetic fields in micromagnetic simulations to drive skyrmion breathing modes in a synthetic antiferromagnet and combine these with an in-plane, static magnetic field to excite skyrmion motion in a wigglelike fashion. We investigate this motion as a function of frequency, and relate it to the intrinsic breathing modes of these skyrmions. We use this understanding of the coupling between velocity and breathing mode frequency to understand the true relationship between the skyrmion velocity and the antiferromagnetic interlayer exchange coupling strength. Finally, we use the additional knowledge of this mechanism to discuss the differences between the previous electric-field driven skyrmion motion [47] and our work. The additional understanding of the relationship between the skyrmion breathing modes and the velocity can be used in applications to modulate the speed of the skyrmion using only the microwave frequency, and has particular relevance to the emerging field of skyrmion magnonics [48]. The emission of spin waves by a domain wall driven by microwave magnetic fields has also very recently been demonstrated [46]. This, together with the similarly recent imaging of spin waves in a synthetic antiferromagnet [49], paves the way to the experimental realization of our method.

II. METHODS

The synthetic antiferromagnet multilayer presented in this paper was studied using the micromagnetic solver MUMAX3 [50]. MUMAX3 is a finite difference numerical solver for the Landau-Lifshitz-Gilbert (LLG) equation that calculates the spatial and time dependence of the magnetization **m** in a simulation [50]. The LLG equation is given by

$$\frac{d\mathbf{m}}{dt} = -|\gamma_0|\mathbf{m} \times \mathbf{H}_{\text{eff}} + \alpha \mathbf{m} \times \frac{d\mathbf{m}}{dt},\tag{1}$$

where **m** is the magnetization unit vector, α is the Gilbert damping parameter, and \mathbf{H}_{eff} is the effective magnetic field. The effective magnetic field is proportional to the differential of the total micromagnetic energy U, given by

$$\mathbf{H}_{\text{eff}} = -\frac{1}{\mu_0 M_s} \frac{\delta U}{\delta \mathbf{m}}.$$
 (2)

Here μ_0 is the permeability of free space which is $4\pi \times 10^{-7} \, \mathrm{N \, A^{-2}}$, and M_s is the saturation magnetization of the system. The micromagnetic energy U includes the usual energy terms that describe the interaction with an external magnetic field, the effects of the demagnetization field, the Heisenberg exchange. In these simulations we consider a single anisotropy energy term perpendicular to the plane of the field. This is given by

$$U_{\text{Anis}} = -K_{\text{u}} \int (\mathbf{u} \cdot \mathbf{m})^2 dV, \tag{3}$$

where $K_{\rm u}$ is the anisotropy constant, and ${\bf u}$ is a unit vector denoting the direction of the ansiotropy, in this case, along the vector perpendicular to the film plane. In addition, we consider an interfacial DMI term of the form

$$U_{\text{iDMI}} = D \int [m_z(\nabla \cdot \mathbf{m}) - (\mathbf{m} \cdot \nabla)m_z]dV, \qquad (4)$$

where D is the DMI constant. Finally, we add a custom energy term to the simulation to model the indirect interlayer exchange coupling, given by

$$U_{\text{RKKY}} = -\sigma_{\text{RKKY}} \int (\mathbf{m_1} \cdot \mathbf{m_2}) dV, \tag{5}$$

where the subscript of \mathbf{m} denotes the layer number, and σ_{RKKY} is the coupling energy. The system is antiferromagnetic for $\sigma_{RKKY} < 0$.

The simulation is set up with exchange stiffness $A = 15 \times$ 10^{-12} J/m, saturation magnetization $M_s = 580 \times 10^3$ A/m, uniaxial anisotropy constant $K = 7 \times 10^5 \text{ J/m}^3$, interfacial DMI $D = 3 \times 10^{-3} \text{ J/m}^2$ and Gilbert damping parameter $\alpha = 0.01$. These values represent typical generic parameters of metallic multilayers with DMI that are usually chosen for synthetic antiferromagnets hosting skyrmions [51]. They are also chosen specifically to mirror those used in Ref. [47] in order to better compare results. The system was initialized with an in plane x-y cellsize of 1.5625 nm and an out-ofplane z cell size of 0.4 nm. The configuration of cells was $256 \times 256 \times 4$ cells, for a total layer width and length of 400 nm and a total stack thickness of 1.6 nm. Only two of the layers were magnetic, with the remaining two layers not contributing to the simulation other than to mirror the spatial separation of the magnetic layers as in a real system.

To measure the frequency response of the system, it was excited at t = 0 with a sinc magnetic field along the z axis with a cutoff frequency of f = 100 GHz of the form

$$H_z = H_0 + H_1 \frac{\sin(2\pi ft)}{2\pi ft},$$
 (6)

where H_0 is an optional static field, H_1 is the magnitude of the sinc field, 0.5 mT unless otherwise specified. This was used as it is a top-hat function in Fourier space, and so excites all modes equally up to its cutoff frequency. Simulations were

then run for 10–20 ns, and the magnetizations of each layer were recorded. The change in magnetization, based on the spatial average of the magnetization in each layer at time t, $\langle m_z(t) \rangle$ is calculated as

$$\delta m_z = \langle m_z(t) \rangle - \langle m_z(0) \rangle. \tag{7}$$

The frequency response of the system is then calculated using the power spectral density (PSD), which is given by the Fourier transform of δm_z multiplied by its complex conjugate

$$PSD = \left| \int_0^{t_0} \delta m_z e^{2\pi f t} dt \right|^2. \tag{8}$$

To excite the skyrmion motion—unless otherwise specified—a static in-plane field of 0.5 T is used, together with a static out-of-plane field of 50 mT and an out-of-plane microwave excitation field of 20 mT. The static in-plane field is chosen to be 0.5 T to be consistent with previous work studying skyrmion motion driven by excitation with an electric field [47]. Likewise the choice of the 50 mT static out-of-plane field is in line with previous work on skyrmion breathing driven by a magnetic field [39,40]. As discussed in Ref. [39], this small static field serves to aid in the observation of the in-phase skyrmion breathing mode, but does not otherwise alter the behavior of the breathing modes for fields much smaller than the saturation field, as is the case for our chosen value (see note S1 [52] for measurement of the saturation field.). The microwave excitation field is smaller than that used by other works [15] but a comparable order of magnitude. In order to track the motion of the skyrmion, for each timestep we calculate the guiding center \mathbf{R}_{Sk} of each magnetic layer, given by

$$\mathbf{R}_{Sk} = \frac{\int \mathbf{r}q \, dx dy}{\int q \, dx dy},\tag{9}$$

where ${\bf r}$ is the position vector of each cell, and q is the topological charge density

$$q = \mathbf{m} \cdot \left(\frac{\partial \mathbf{m}}{\partial x} \times \frac{\partial \mathbf{m}}{\partial y}\right),\tag{10}$$

such that the topological charge of the skyrmion would be $Q = (1/4\pi) \int g dx dy$, which will be equal to 1 and -1 for the two skyrmions. We also note here that throughout this paper, quantities of the skyrmions are often plotted separately for the skyrmions in each layer, and also split further for the behavior of that quantity along the x and y axes. Throughout this paper we will denote the skyrmion in the bottom layer (layer 1) of the SAF with the color blue, and the skyrmion in the top layer (layer 2) with the color black. Also see Fig. 1(a) for a sketch of the simulation stack. We further subdivide this into the behavior along the x axis, which will be represented by diamond-shaped points, and the behavior along the y axis, which will be denoted by circular points. We also adopt the notation $Sk_{n,i}$ to label these quantities, where n denotes the layer number and i is either x or y. This notation and color scheme is used throughout.

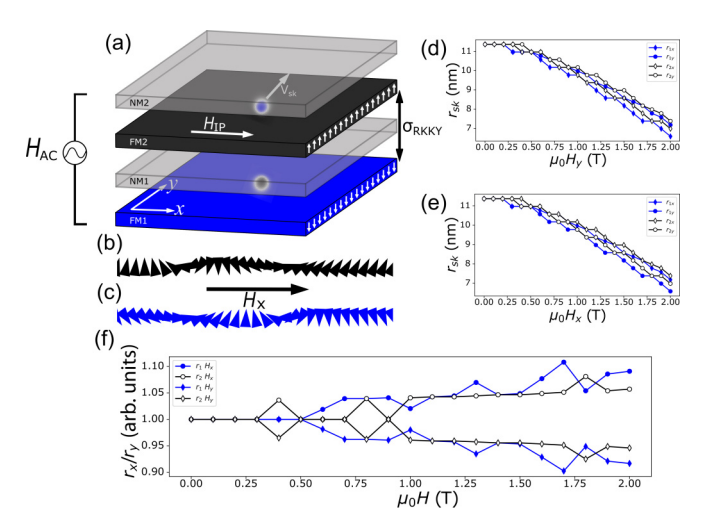


FIG. 1. Illustration of simulation setup and characterization of skyrmion radius as a function of field. (a) Illustration of the simulated multilayer. Two ferromagnetic (FM) layers, labeled FM1 and FM2 are coupled together antiferromagnetically through a non-magnetic (NM) spacer layer. An in-plane field ($H_{\rm IP}$) causes the skyrmion to elongate, while the sinusoidal driving field causes it to emit spin waves and move perpendicular to $H_{\rm IP}$. (b) and (c) show the cross sections of the two skyrmions in layers 1 and 2 along the x axis in an in-plane magnetic field along the x axis of 1.7 T. The effect of the in plane field is shown on the radius of the two coupled skyrmions for field along the y axis in (d) and field along the x axis in (e). The ratio of the radius along the x and y axes of each skyrmion for each field orientation is shown in (f). The quantization is related to the cell size of the simulations.

III. STATIC AND DYNAMIC CHARACTERIZATION

A. Effect of in-plane field on skyrmions

The effect of a static in-plane field on the skyrmion radius is shown in Figs. 1(b)-1(e) for an antiferromagnetic interlayer exchange coupling strength of -0.3 mJ/m^2 in a static outof-plane field of 50 mT. For this antiferromagnetic interlayer exchange coupling strength, the interlayer coupling is sufficiently strong to overcome the effects of the out-of-plane field and so the two skyrmions have equal radius in zero in-plane field $H_{\rm IP}$. As the field increases above ~ 0.3 T, the skyrmions in each layer begin to both stretch and shrink. This shrinking is caused by the in-plane field pulling the cores of the two skyrmions apart laterally—as shown in Figs. 1(b) and 1(c)—which introduces a breaking of the antiferromagnetic interlayer coupling between spins inside the skyrmion. Thus, the skyrmion size shrinks to minimize this. Because of this, the stretching of the skyrmion is better demonstrated by the ratio between r_x and r_y , as shown in Fig. 1(f). Above fields of ~0.3 T, this behavior starts to change, and steadily changes from 0.5 T onwards, indicating the stretching of the two skyrmions along the direction of the field. On this basis, unless otherwise specified, an in-plane field of 0.5 T is chosen for further simulations which causes a modest deformation of the skyrmion, and also allows for better intercomparison of results with Ref. [47]. Simulations of the full hysteresis loops are shown in note S1 [52]. The saturation field along the x and

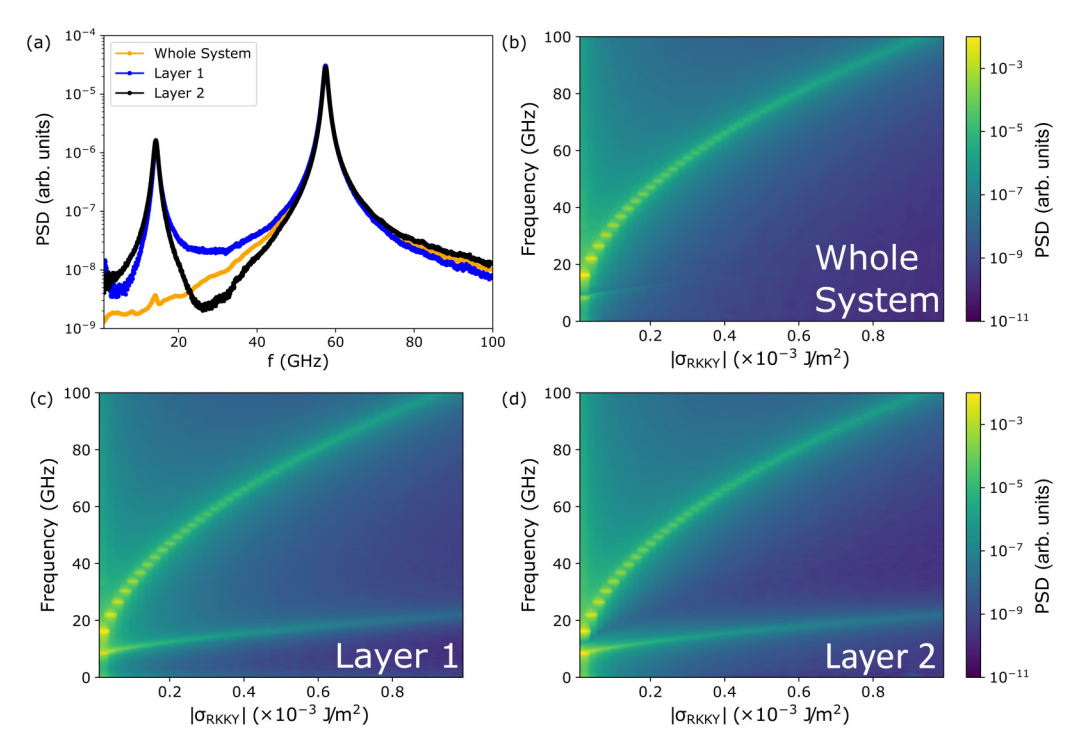


FIG. 2. Skyrmion frequency response as a function of frequency and antiferromagnetic interlayer exchange coupling strength. (a) Shows the frequency response for an interlayer exchange coupling strength of -0.3 mJ/m^2 . (b)–(d) show color maps of the response as a function of interlayer exchange coupling strength, denoted as $|\sigma_{RKKY}|$. (b) Shows the response of the entire simulated system, whereas (c) and (d) show the response when calculating the PSD of just the magnetization of the cells of layers 1 and 2, respectively. (b), (c), and (d) have a common color bar.

y axes is 4.3 T, demonstrating that this in-plane field is only a modest $\sim 10\%$ of saturation.

B. Skyrmion breathing modes

Before the motion of the skyrmions is induced, we first study the breathing modes of the system following the approach of Ref. [39]. As outlined in the methods, the system is first initialized with a Néel-type skyrmion in each layer and allowed to relax in a static out-of-plane field of 50 mT. Then a sinc pulse of amplitude 0.5 mT and frequency 100 GHz is applied at time 0 and the simulation is run for 20 ns. The results of this are shown in Fig. 2. Figure 2(a) shows an illustration of the skyrmion frequency response with an interlayer exchange coupling strength of -0.3 mJ/m^2 for the two individual layers as well as the whole system. Because periodic boundary conditions were used for these simulations, there is no curling of the magnetization at the edge, and so there are no modes arising from this and the frequency response seen here comes entirely from the skyrmion [40]. We see at \sim 14 GHz there is a mode present in each of the individual layers, whereas, in the total system, there is almost no response. At the higher frequency mode at \sim 57 GHz, there is a response in all three plots. This has been well studied [39,40]; the difference arises from the interplay between the two skyrmions at each mode. When excited at the lower mode, the two skyrmions breathe in phase with each other, and so at any time t, spins in each magnetic layer are coupled antiparallel over the whole lateral extent of the system, and so the net moment is always canceled. Conversely at the higher frequency mode, the two

skyrmions breathe in antiphase, and so at any time t there is always a small net moment originating from the difference in size of these two skyrmions, and thus there is an observable peak in the frequency response of the system as a whole. Heat maps of the frequency response of the whole system and the two individual layers are then shown in Figs. 2(b)-2(d). There is a considerable variation in the frequencies of the two peaks, especially that of the second as a function of the interlayer antiferromagnetic exchange strength.

IV. ALL MAGNETIC FIELD DRIVEN SKYRMION MOTION

A. Skyrmion motion driven by the addition of an in-plane magnetic field

Considering the static and dynamic characterization of skyrmions in the simulated system described in Secs. III A and IIIB, we now move on to describing the effect of an in-plane field together with an excitation field on the motion of the SAF skyrmion. The frequencies of the two peaks of Fig. 2(a) are found by fitting the data to a Lorentzian lineshape to be 14.3 and 57.4 GHz. A sinusoidal driving field is then used at the higher frequency to drive the skyrmion together with a static out-of-plane field of 50 mT as discussed in Sec. III B. This is also done with an in-plane static field of 0.5 T. The results of this are shown in Fig. 3. Figure 3(a) shows the x and y positions of the guiding centres of the skyrmions in each layer as a function of time for 10 ns. We see that—while the skyrmion moves steadily along the y axis at a seemingly constant rate—the x-axis motion proceeds in an oscillatory fashion with an oscillation frequency of ~1 GHz, with an

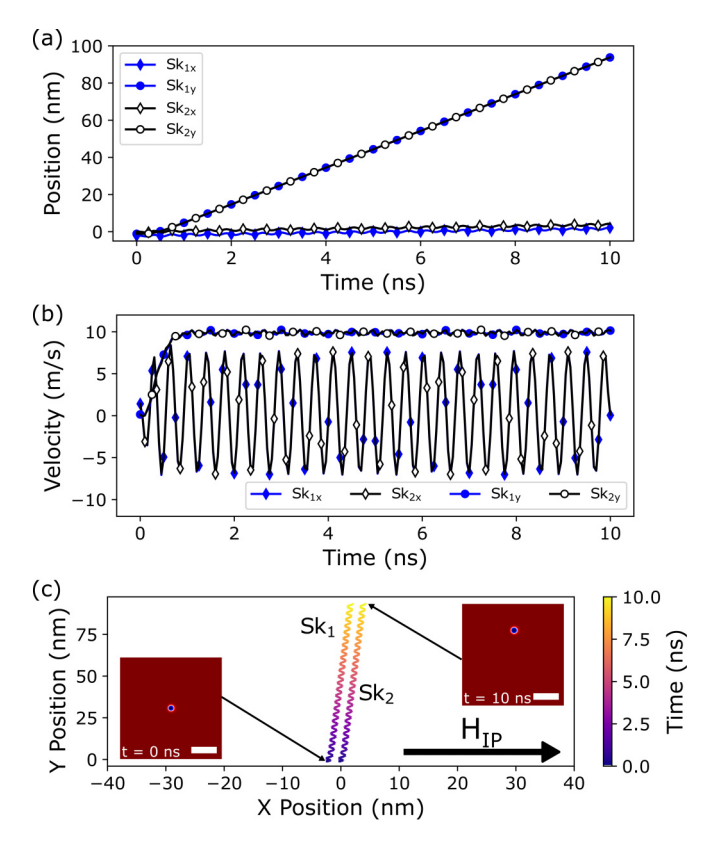


FIG. 3. In-plane field-driven skyrmion motion in a field of $0.5 \,\mathrm{T}$ along x, driven at a frequency of 57.4 GHz. (a) shows the x and y positions of the skyrmion guiding center for both the skyrmions in layers 1 and 2 of the SAF. Panel (b) shows the calculated velocities of these guiding center x and y positions as a function of time. Points on the lines in (a) and (b) are deliberately undersampled to see both the datapoints of layers 1 and 2. (c) shows the trajectory of both skyrmions, with the y positions of each skyrmion plotted against the x position. The color gradient of each line denotes the time, which is shown on the color bar to the right of the panel. The two insets show the position of the skyrmion in one of the layers at the start ($t = 0 \,\mathrm{ns}$) and end ($t = 10 \,\mathrm{ns}$) of the simulation. Scale bar is 100 nm. The arrow in the bottom right shows the direction of the in plane static field.

additional very small net movement along the x axis. This can also be visualized with the trajectories of the two skyrmions shown in Fig. 3(c), together with the insets showing the initial and final positions of the skyrmion. We see that the skyrmions move in a wigglelike fashion, the first report of this kind of motion in a synthetic antiferromagnet. This is also unlike the motion observed in Ref. [47] but similar to the trajectories in similar ferromagnetic systems reported in Ref. [45]. The position as a function of time is used to calculate the x and y velocities of each skyrmion as a function of time, which is shown in Fig. 3(b). The y velocities ramp up from 0 for the first ~ 1 ns, before maintaining a steady value of ~ 10 m/s for the rest of the simulation time. Meanwhile, the x velocities oscillate around 0, driving the wigglelike motion. To calculate the average velocities presented later, an average is taken of the y-axis velocity once it reaches its steady value, here around 3 ns into the simulation time.

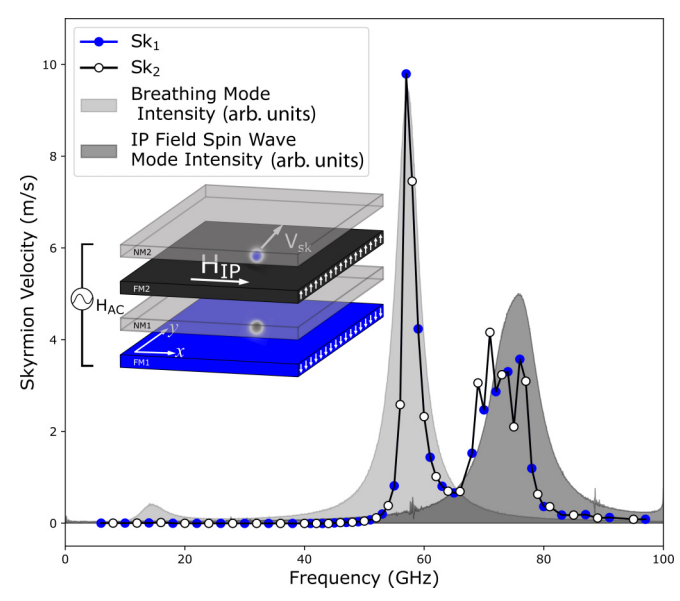


FIG. 4. Velocities of the two skyrmions as a function of frequency of the driving field. Datapoints are deliberately undersampled so that both datasets are visible. The intensity of the breathing modes from Fig. 2 is overlaid with light grey shading and rescaled to match the peak amplitudes. The power spectral density of the spin wave mode arising from the canted spins in the IP field (see note S2 [52]) is also overlaid in a dark grey shading. Inset shows the same schematic from Fig. 1 to illustrate the directions of the magnetic fields and the direction of skyrmion motion.

B. Skyrmion velocity coupled to out-of-phase breathing

The average velocity as a function of frequency is presented in Fig. 4 for an antiferromagnetic interlayer exchange coupling strength of $-0.3 \, \text{mJ/m}^2$, over a range of frequencies from 6 GHz to 97 GHz. Added for comparison is the PSD of the breathing modes from Fig. 2(a) rescaled to allow comparison with the calculated velocities. There is a strong overlap between the peak velocity of the skyrmion and the peak in the breathing mode intensity, suggesting a coupling between the breathing mode and the velocity. However, perhaps surprisingly, there is no similar peak when driving the skyrmion motion at the lower frequency of the in-phase peak.

Between frequencies of \sim 70 and \sim 80 GHz in Fig. 4(a) above the out-of-phase breathing mode resonant frequency there is a second broader peak in velocity that is seemingly not related to any skyrmion breathing mode. This is reminiscent of the higher frequency hybridization of skyrmion breathing with spin wave modes of ferromagnetic [36] and synthetic antiferromagnetic [39] nanodots that has been previously observed. However, as discussed in Sec. II, in this simulation, periodic boundary conditions in the x-y plane are used. This excludes such spin wave resonant modes, since they originate from spin canting at the edges of the simulation, which the application of periodic boundary conditions removes. We instead suggest that this higher frequency broad peak in velocity arises from exciting a hybrid mode between the skyrmion breathing and a spin wave mode arising from the canting of spins in the applied in-plane field. Because of the motion that would be induced by performing the simulations used to generate Fig. 2 in an in-plane field, this is difficult to show directly.

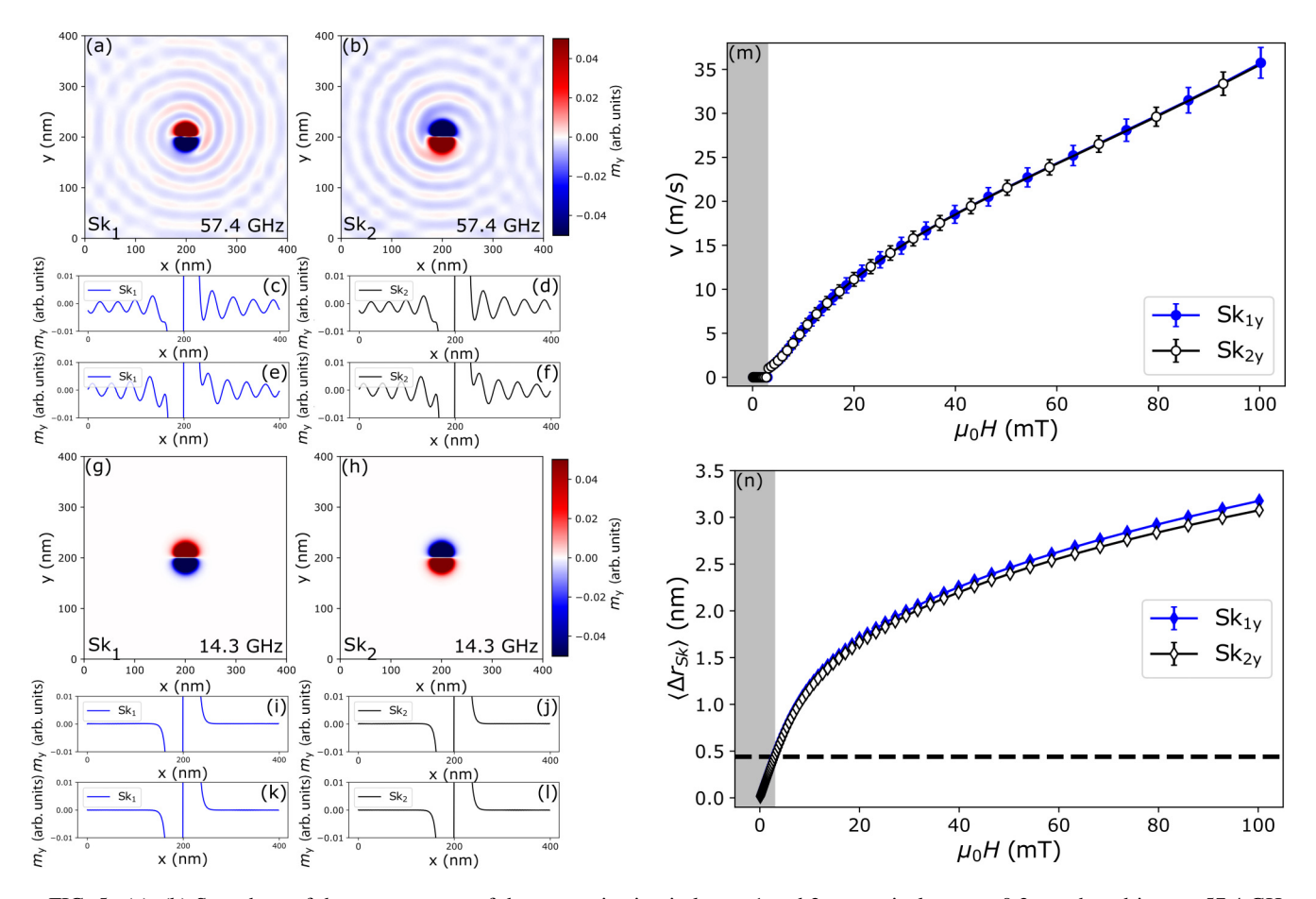


FIG. 5. (a), (b) Snapshots of the *y* component of the magnetization in layers 1 and 2 respectively at t = 0.2 ns when driven at 57.4 GHz. The colormap has been windowed to show the spin wave emission. [(c) and (d)] Show line cuts through the center of the skyrmion from (a) and (b), while [(e) and (f)] show the equivalent line cuts through the center of the skyrmion in the case where the in-plane field is removed, but still at 0.2 ns after the start of the simulation with the same out-of-plane driving field. (g)–(l) are all the same but with a 14.3 GHz driving field. [(g) and (h)] Are snapshots of layers 1 and 2 respectively at 0.2 ns, (i) and (j) are line cuts through (g) and (h), and (k) and (l) are the equivalent line cuts in the absence of an in-plane field. (m) shows the average skyrmion velocity when driven with a static in-plane field of 0.5 T as a function of the out-of-plane excitation field. The gray shaded region denotes the field range below which there is no motion. Datapoints are deliberately undersampled so that both datasets are visible. (n) shows the average peak-to-peak variation in the skyrmion radius when breathing as a function of the amplitude of the out-of-plane field in the absence of an in-plane field. The gray shaded region is taken from (m) and the black dashed line is a guide to the eye to separate radii measured with excitation fields above and below this region. Note that the error bars on these series are too small to be visible.

However, in note S2 [52], we show and discuss simulation of the PSD in the presence of an in-plane field but without a skyrmion, which yields a peak of similar center frequency and width to this second peak in velocity. The power spectral density arising from this is shown in Fig. 4 as the darker gray shaded region, with a peak at higher frequencies, approximately matching the corresponding peak in velocity. This is discussed in detail in supplementary note S2 [52], however it clearly demonstrates that the peak in velocity arises from hybridization between the skyrmion breathing mode and the spin wave resonance of the canted spins when an in-plane field is introduced.

C. The effect of the spin wave emission amplitude

It has been discussed that the motion of the skyrmions in these systems is driven by spin wave emission [16,45,47], however, the mechanism of this spin wave emission has not been investigated in detail. This emission is represented more clearly in Figs. 5(a) and 5(b), which show the skyrmion when driven at 57.4 GHz in a 0.5 T in-plane magnetic field at 0.2 ns after the start of the simulation; around the onset of skyrmion motion. There is some interference present because of the periodic boundary conditions. Similarly Figs. 5(g) and 5(h) show the same situation when the system is driven with a field of 14.3 GHz, the frequency of the in-phase breathing mode. These images are complemented by videos S1 and S2 [52] that show this spin wave emission over the first 1 ns of the simulation in the presence of an in-plane magnetic field. To further illustrate the spin wave emission, each of these pairs of colormaps are complemented with line cuts that are take through the center of the skyrmion, shown in Figs. 5(c) and 5(d) for the 57.4 GHz case and Figs. 5(i) and 5(j) for the 14.3 GHz case. These line cuts are in turn complemented by videos S3 and S4 [52], which again show this profile over the first 1 ns of the simulation, in an in-plane magnetic field of

0.5 T, driven by an out-of-plane oscillating field of 20 mT, at 57.4 and 14.3 GHz in videos S3 and S4 [52], respectively. These videos show that the spin waves are emitted at the maxima of the oscillations in the skyrmion radius. This is remarkably similar to the experimental demonstration of spin wave emission from an oscillating domain wall [46], where the oscillating wall "knocks" the domain interior, stimulating spin waves [46]. It is clear from Figs. 5(a), 5(b) and 5(g), 5(h) that the main difference between being driven at 57.4 GHz—where there is skyrmion motion—and at 14.3 GHz where there is no skyrmion motion—is the amplitude of the emitted spin waves. It is well understood that the oscillations in radius at the out-of-phase breathing mode are considerably larger than at the in-phase breathing mode [39,40]. We suggest that the primary factor determining the strength of the emitted spin waves is the magnitude of the change in radius. This is in turn affected by the magnitude of the driving field. However, for the same magnetic field amplitude, this will increase when tuning onto a skyrmion breathing mode resonant frequency, and will also be considerably larger for the out-phase breathing mode frequency than the in-phase breathing mode frequency.

To investigate this in more detail, we examine the amplitude of the variation in radius in the absence of an in-plane magnetic field. We do this because the deformation of the skyrmions—as shown in Fig. 1—will affect the accuracy of determining the change in radius. Figs. 5(e) and 5(f) show snapshots of the same slice through the center of the skyrmion at the same time as Figs. 5(c) and 5(d) at the same driving field frequency of 57.4 GHz, but without the in-plane field. Likewise, Figs. 5(k) and 5(l) show the same, but at a driving field frequency of 14.3 GHz, equivalent to Figs. 5(i) and 5(j) but without the in-plane magnetic field. Both of these sets of snapshots are supported by videos S5 and S6 which show the same data over the first 1 ns of the simulation. For a detailed description of all of the supplementary videos see note S3 [52].

In Figs. 5(m) and 5(n), we show a simultaneous study of the skyrmion velocity [Fig. 5(m)] and the magnitude of the variation in radius [Fig. 5(n)], both as a function of the magnitude of the driving microwave magnetic field at a frequency of 57.4 GHz. For details of how the average change in radius was calculated, see note S4 [52]. In Fig. 5(m), at fields above ~20 mT there is a clear linear relationship between the velocity and the driving field. However, below fields of \sim 20 mT, the skyrmion velocity drops off faster towards 0 m/s, and there is no motion below driving fields of \sim 3 mT. This region of no skyrmion motion is represented with the grey shaded box. Since this is a simulated system with no pinning, this is clearly an intrinsic effect of their being an insufficient spin wave emission amplitude to drive motion. Likewise, examining the magnitude of the variation in radius in Fig. 5(n), we draw the same threshold field for skyrmion motion from Fig. 5(m) also as a grey shaded box. For these magnetic parameters, we are then able to define a variation in radius of the skyrmions below which there is no motion of $\langle \Delta r_{\rm Sk} \rangle = 0.44$ nm, or $\sim 3.5\%$ of the static skyrmion radius r_0 .

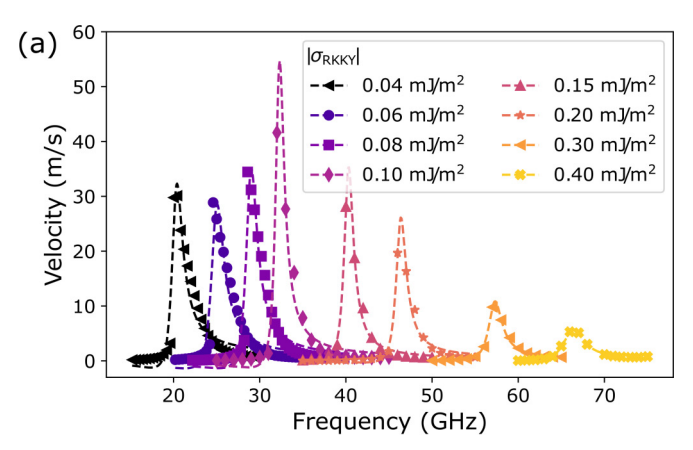
To summarize, the motion of the skyrmions is primarily driven by the emission of spin waves. As we have shown, this spin wave emission occurs when the magnitude of the skyrmion expansion is at its widest. The results of Fig. 5 show that there is a minimum variation of skyrmion radius required to emit spin waves that are strong enough to drive motion. This radius variation will itself be dependent on the driving field; however, the relationship between radius variation and driving field will be different at the two resonant breathing modes. For this reason, we have determined empirically that it is more accurate to define a minimum variation in radius rather than a minimum driving field. This interpretation also explains the absence of skyrmion motion at the resonant frequency of the in-phase breathing mode in Fig. 4(a). The variation in skyrmion radius at this frequency is well understood to be significantly smaller for the same driving magnetic field amplitude than when driven at the out-of-phase resonant frequency [39,40]. Performing the same analysis on the variation in radius of the in-phase breathing mode when driven by a out-of-plane excitation field of 20 mT gives a $\langle \Delta r_{\rm Sk} \rangle$ of 0.286 ± 0.002 nm, below this threshold for motion.

Furthermore, by performing these simulations, we have also developed an understanding of the relationship between skyrmion velocity and microwave power. Figure 5(m) shows the velocity of the skyrmion as a function of the amplitude of the driving field, which is simply a representation of the microwave power driving the spin wave emission. As we have already discussed, for the lowest fields there is no observable skyrmion motion, before a non-linear ramp up in velocity between 3 and 20 mT, after which there is a linear relationship between skyrmion velocity and microwave power. This result will help to inform experimental study of skyrmion motion driven by this effect, where the exact relationship between microwave power and magnetic field amplitude will depend on factors such as fabrication of waveguides and losses in connectors, among others.

D. The effect of antiferromagnetic interlayer exchange coupling

With our new understanding of the coupling between skyrmion velocity and the frequency of the out-of-phase breathing mode, we now move to studying it as a function of the antiferromagnetic interlayer exchange coupling strength. The results of measuring the velocity as a function of frequency at different coupling strengths σ_{RKKY} are presented in Fig. 6(a). The data presented here has been trimmed around the frequency of the out-of-phase breathing mode for clarity, so the broad peak in velocity associated with the in-plane field is not shown. This however follows the same behavior—albeit shifted in frequency—as the one for $\sigma_{RKKY} = -0.3 \text{ mJ/m}^2$ shown in Fig. 4(a) and discussed in note S2 [52]. The extracted values of skyrmion velocity as a function of frequency are fitted to an asymmetric Lorentzian line shape, chosen for its empirical match to the data, which allows us to extract a value for the peak velocity. This peak velocity as a function of σ_{RKKY} is then shown in Fig. 6(b).

In Ref. [47], Qiu *et al.* discuss the variation of the skyrmion velocity (driven by modulations in anisotropy) as a function of σ_{RKKY} , and propose this as a way of modulating the skyrmion velocity. Our results show that while this variation in velocity with σ_{RKKY} is true at a fixed frequency, it is not fundamentally related to the value of σ_{RKKY} . Instead, we have clearly shown that the magnitude of the velocity is correlated to the



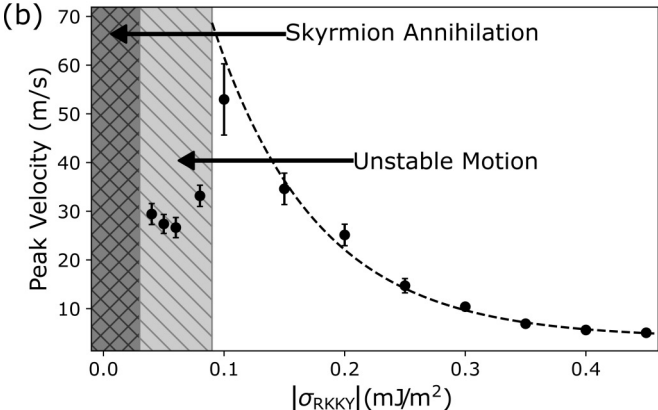


FIG. 6. (a) Skyrmion velocity as a function of frequency plotted for varying antiferromagnetic exchange coupling σ_{RKKY} . Dashed lines show fits to an asymmetric Lorentzian function used to extract the peak velocity. All simulations were performed with static fields of 50 mT out-of-plane and 0.5 T in-plane, along with a microwave driving field of 20 mT. (b) The extracted peak velocities as a function of the coupling strength. The regime where at least one skyrmion is annihilated when driven on resonance is cross-hatched, while the coupling regime where the skyrmions move unstably is single hatched. The dashed line shows an inverse cube law as a guide to the eye for peak velocities in the high coupling strength regime.

size of the oscillations in skyrmion size. This modulation of the skyrmion size is itself a result of tuning onto the intrinsic frequency of the out-of-phase breathing mode. Thus, by examining the peak velocity value for each σ_{RKKY} we can understand the true impact of the antiferromagnetic interlayer exchange coupling strength on the skyrmion motion. We define three principal regimes of the skyrmion velocity when driven on the resonant frequency.

First, we define the skyrmion annihilation regime for low values of σ_{RKKY} , smaller in magnitude than $\sim -0.03 \text{ mJ/m}^2$. Here the skyrmions are stable in the static case and skyrmion motion is still possible when driving with microwave magnetic fields. However, when it is driven close to the resonant frequency, the oscillations of the skyrmions at this field strength are sufficiently large to drive the annihilation of the skyrmions in at least one of the layers. Clearly the strength of the antiferromagnetic coupling is insufficient to stabilize the two skyrmions as a topological object.

TABLE I. Compilation of reported antiferromagnetic interlayer exchange coupling strengths from several previous studies.

Material system	Magnetic texture	Coupling strength (mJ/m²)	Reference
Co/Ru/Pt/Co Pt/Co/CoFeB/ Ir/Co/CoFeB/W	Skyrmions Skyrmions	-0.23 -0.13	[25] [32]
Co/Ni/Co/Ru/ Co/Ni/Co	Domain walls	-0.5	[28]
[CoFeB/Ru/Pt/ CoB/Ru/Pt] _{×5}	Domain walls	-0.018	[30]

For intermediate values of σ_{RKKY} between ~ -0.03 mJ/m² and < -0.1 mJ/m², the strength of the coupling is sufficient to prevent the annihilation of the skyrmions, however their oscillations are substantially more unstable than at higher coupling strengths, and the *x*-axis trajectories (the direction orthogonal to the principal direction of motion) of the two guiding centres drift apart by up to several nanometres over the course of the simulations. We suggest that this disparity between the two skyrmions restricts their ability to move together efficiently, and we see that the peak velocity over this narrow region of σ_{RKKY} is almost completely flat. In the simulation at $\sigma_{RKKY} = -0.08$ mJ/m², there is a small uptick in velocity as we transition to the high σ_{RKKY} regime.

For values of σ_{RKKY} from -0.1 mJ/m^2 and increasing in magnitude, we see a very clear inverse relationship between the peak skyrmion velocity and the strength of the antiferromagnetic interlayer exchange coupling. The two skyrmions move together with regular oscillations in size for the whole simulation space. The decrease in velocity with σ_{RKKY} can be clearly understood as a consequence of the constraining effect of the antiferromagnetic coupling strength, which as it increases will reduce the magnitude of the oscillations in skyrmion radius, and in turn reduce the velocity.

While experimental measurements of skyrmions and other magnetic textures are limited in synthetic antiferromagnets, several studies report observations of skyrmions and domain walls. In Table I, we summarize the reported antiferromagnetic coupling strengths from a literature search of DMI stabilized textures in synthetic antiferromagnets. The fact that most of these reported values fall in the range of σ_{RKKY} in our study where we report skyrmion motion suggests that this method would be appropriate for driving SAF skyrmions in a future computing device.

V. SKYRMION MOTION IN SYNTHETIC FERRIMAGNETS

In experimental SAFs, it is often difficult to grow magnetic layers with perfect compensation, especially when using layers of multiple compensations [30,53]. To extend our understanding of the effects presented in this paper, we consider synthetic ferrimagnets, where we introduce a decompensation of the magnetization of one of the two layers. The measurement of the breathing modes has already been demonstrated in Ref. [39], where simulation of a synthetic

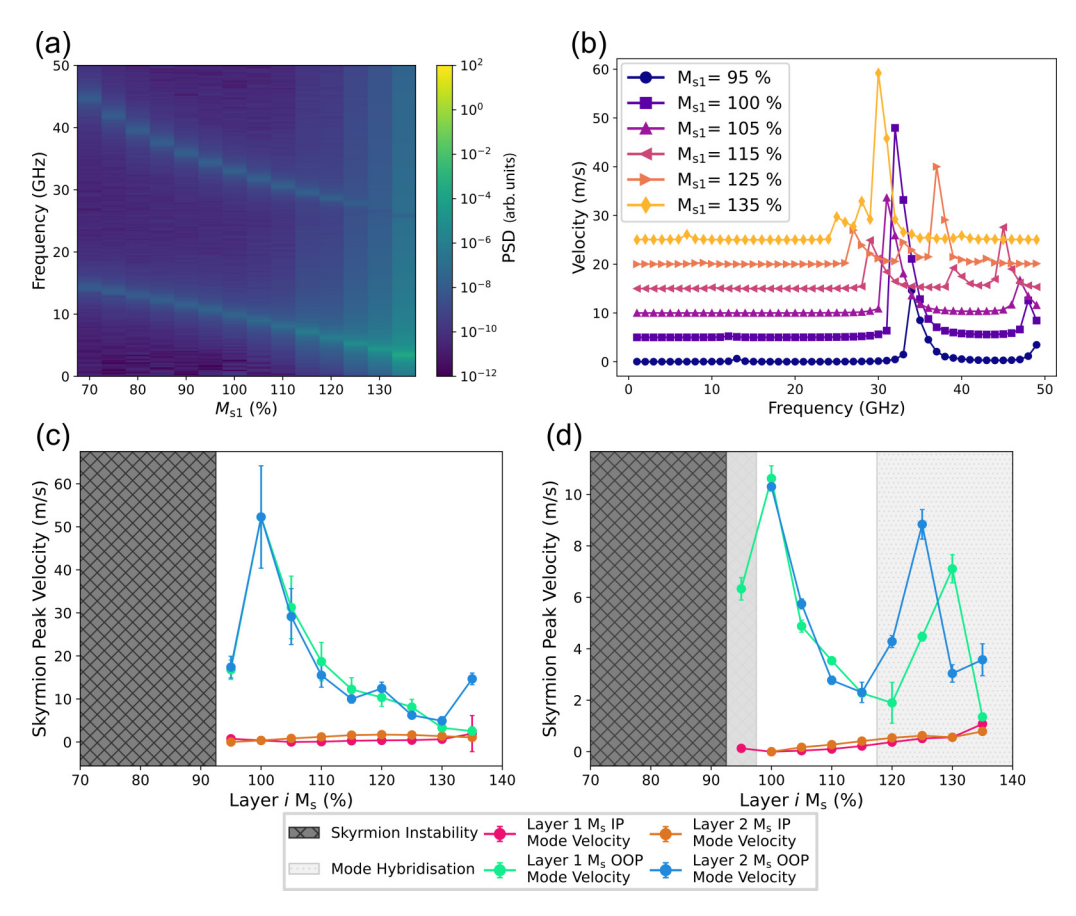


FIG. 7. Breathing modes and motion as a function of decompensation of one of the magnetic layers, expressed as a percentage of the original M_s value of 580×10^3 A/m. (a) The PSD of the system, varying the M_{s1} for an antiferromagnetic interlayer exchange coupling of -0.1 mJ/m². (b) Plots of the velocity as a function of frequency for several selected values of decompensation of layer 1, for the same antiferromagnetic interlayer exchange coupling. Note that each dataset has been deliberately offset to better see the individual trends. [(c) and (d)] Values of the peak velocities at both the IP and OOP breathing mode peaks as a function of decompensation of the M_s of both layer 1 and layer 2, for antiferromagnetic interlayer exchange coupling strengths of -0.1 and -0.3 mJ/m², respectively. Note that (c) and (d) share a common legend, seen below both panels.

ferrimagnet (SFiM) was achieved by varying the M_s of one layer. Similarly, the current driven dynamics of skyrmions in angularly decompensated SAFs have been studied by varying the ration of $M_{\rm s1}/M_{\rm s2}$ of the two layers [54]. Here, we follow this method, and examine our system at two characteristic antiferromagnetic interlayer exchange coupling strengths, while varying the M_s of each layer individually by $\pm 30\%$ of its original value. We note that in most experimental SAFs the decompensation between the magnetizations of each layer is $\leq 10\%$ [30,53]. Thus our chosen range is adequate to describe experiments well, while also extending our understanding to higher decompensations. Throughout we conduct every simulation by fixing the M_s of one layer to its original value, and vary the M_s of the second layer. We use the labels M_{s1} and $M_{\rm s2}$ to denote these two values, and for every simulation we consider the case of varying each of these two quantities. The breathing mode frequencies for an antiferromagnetic interlayer exchange coupling strength of $\sigma_{RKKY} = -0.1 \text{ mJ/m}^2$ and a variation of $M_{\rm s1}$ by $\pm 30\%$ are shown in Fig. 7(a) as a heatmap. The PSD here is taken for only layer 1 of the system, in order to be able to observe the signal of the in-phase breathing mode, however the behavior of the mode frequencies is the same for the PSD of layer 2 and the whole

system. In general, the resonant frequencies of both the inphase and the out-of-phase modes both decrease as the value of $M_{\rm s1}$ increases. This matches the results of Ref. [39], where it was shown that in compensated SAFs, the frequencies of the resonant modes decrease with $M_{\rm s}$. Likewise, our results match those considering SFiM systems [39], where it was shown that the frequencies of the resonant modes continue to follow this trend even when the variation in $M_{\rm s}$ is restricted to only one of the magnetic layers.

With this understanding of the behavior of the two resonant modes, we move on to consider the velocity of the skyrmions in uncompensated systems. The velocity as a function of frequency for several representative values of $M_{\rm s1}$ is shown in Fig. 7(b). These data are for an antiferromagnetic interlayer exchange coupling strength of $\sigma_{\rm RKKY} = -0.1~{\rm mJ/m^2}$. Here, each dataset is deliberately offset along the y axis to be able to see the individual trends. It is clear that the velocity at the out-of-phase peak is lower than at full compensation (see Fig. 6 for the measurement at this value of $\sigma_{\rm RKKY}$), and this decreases as a function of the decompensation of $M_{\rm s1}$. Conversely, at the highest decompensations, there is a clear evidence of a small peak in velocity near the in-phase breathing mode frequency. These two effects are better demonstrated in Fig. 7(c), which

shows the measured velocity at each of these two resonant frequencies as a function of decompensation for either of $M_{\rm s1}$ or $M_{\rm s2}$. There is a clear peak in velocity at the out-of-phase resonant frequency when $M_{\rm s1}=M_{\rm s2}$, with skyrmion velocity trailing off at decompensation either side of this value. For $M_{\rm s1,2}$ compensations below 90%, there is no velocity data. This is due to the small value of $M_{\rm s}$. For these low $M_{\rm s}$ values, the increased field amplitude used to drive motion [compared to the excitation of the breathing modes in Fig. 7(a)] annihilates the skyrmions.

As expected, the behavior is reversed when considering the velocity at the in-phase resonant frequency. The velocity is at a minimum value when $M_{\rm s1}=M_{\rm s2}$, and increases away from this. This can be simply understood considering the relationship between skyrmion velocity and breathing amplitude from Sec. IV C. As the difference between the $M_{\rm s}$ of the layers increases, so too will the difference in the oscillation amplitudes of each skyrmion. As we have discussed, this is the main factor determining the skyrmion velocity, and so naturally the velocity increases at this resonant frequency with the increase in unbalance.

Finally, we reproduce this work for a second antiferromagnetic interlayer exchange coupling strength of σ_{RKKY} = -0.3 mJ/m^2 . The measurement of the breathing modes and the individual velocity as a function of frequency plots for each decompensation, analogous to Figs. 7(a) and 7(b) are not shown here, but are instead summarized in note S5 [52]. The velocity of each of the resonant modes as a function of the decompensation is shown in Fig. 7(d). As before, the skyrmion is annihilated when the M_s is below 95% of the original value, demonstrating that this is an intrinsic effect of the low magnetization, rather than a consequence of the weaker coupling present in Fig. 7(c). We see similar behavior at compensations near to $M_{s1} = M_{s2}$, with a peak in velocity at the out-ofphase resonant frequency at full compensation, and increasing velocity at the in-phase resonant frequency with increasing decompensation. However, for values of $M_{\rm s1.2} \ge 120\%$, there is a large degree of variation in the velocity at the out-of-phase resonant frequency. This is due to hybridization between the skyrmion resonant frequency and the spin wave mode of the canted spins discussed in Sec. IV B and note S2 [52]. Here the resonant frequency of the spin wave mode arising from the canted spins decreases faster with increasing $M_{\rm s1,2}$ than the skyrmion breathing mode frequency. Because the two modes are closer in frequency at this interlayer exchange coupling strength, at the higher decompensations, the spin wave mode overlaps with the skyrmion's out-of-phase resonant frequency, and the two effects interact to create more unpredictable spin wave emission. There is also a trace of this effect in Figs. 7(b) and 7(c) for the lower interlayer coupling strength, however it only occurs at the very highest decompensation, and so is less noticeable.

VI. ELECTRIC FIELD DRIVEN SKYRMION MOTION

Previous reports have studied skyrmion motion driven by a microwave electric field [47]. In this work they simulated a similar system with an in-plane magnetic field and drove the motion of skyrmions by adding a microwave frequency perturbation to the anisotropy energy term. This mirrors the

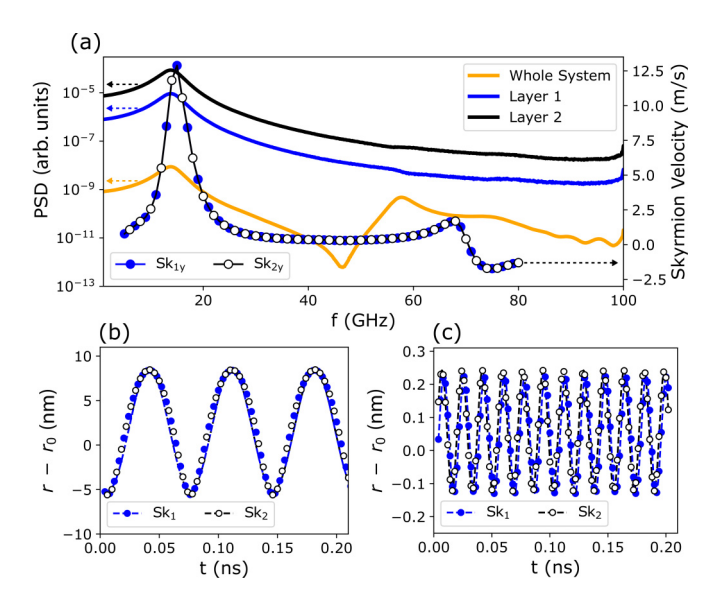


FIG. 8. Examination of the effects of electric field on the skyrmion breathing and velocity at $\sigma_{RKKY} = -0.3 \text{ mJ/m}^2$. This is performed in an out-of-plane magnetic field of 50 mT, and in the case of the motion an in-plane magnetic field of 0.5 T. (a) The PSD of the whole system along with the two individual layers when excited with a modulation of the uniaxial anisotropy of $3 \times 10^4 \text{ J/m}^3$ is plotted on the left axis as a function of frequency. On the right vertical axis, the skyrmion velocity when driven by an electric field as a function of frequency is plotted. (b) and (c) show the variation in radius of the two skyrmions when driven by a sinusoidal electric field at 14.3 and 57.4 GHz, respectively.

voltage controlled magnetic anisotropy that has been demonstrated in thin film multilayers [55]. Reference [47] reported skyrmion velocities as a function of frequency, demonstrating a peak in the skyrmion velocity. However, the relationship between velocity and the resonant frequency of the skyrmion breathing modes was not identified. The frequencies at which they observed their peak velocites were close to the resonant frequency of the in-phase breathing mode that we have shown in Fig. 2. To understand the differences between the mechanisms of magnetic-field driven skyrmion motion and the electric-field driven case previously reported [47], we finally perform some basic simulations using an electric field. In the same way as Ref. [47], the effects of an electric field are simulated by modulating the uniaxial anisotropy with an additional microwave frequency perturbation. We use the same value of 3×10^4 J/m³ for the magnitude of this modulation of the uniaxial anisotropy in all simulations. An interlayer exchange coupling of $\sigma_{RKKY} = -0.3 \text{ mJ/m}^2 \text{ was}$ used, well into the high σ_{RKKY} regime from Sec. IV D. To match the results from Sec. IV B, we perform these simulations in a static out-of plane field of 50 mT as well as an in-plane field of 500 mT in the case of the simulations of motion.

We first examine the breathing modes of the skyrmions, which is shown in Fig. 8(a) for both the individual layers of the system as well as for the system as a whole. Here the features of the PSD occur at the same frequencies as in the magnetic field driven-breathing case, however the presence or lack thereof of each mode in the different layers is different. There

is a strong peak at 14.3 GHz in all three traces, which in the magnetic-field driven case originates from in-phase breathing of the two skyrmions. However, the presence of the peak in the response of the whole system is less straightforward to account for. Alternatively, there is a peak in the whole system at 57.4 GHz where there is only a faint trace in the responses of the individual layers. This behavior is intriguing and merits further investigation.

We also drive the motion of the skyrmions with an electric field of the same magnitude and varying frequency. The measured velocities as a function of the electric field frequency are also plotted on the right-hand axis of Fig. 8(a). Here we observe a strong peak in velocity that is well coupled to the lower frequency breathing mode. Unlike the magnetic field driven case, there is no observable motion at the higher frequency mode, but there is some motion around the frequency of the mode excited by the in-plane field (see supplementary note S2 [52]). To understand this we present in Figs. 8(b) and 8(c) simulations of the radius variation of the skyrmions when driven by a sinusoidal electric field with no in-plane magnetic field at each of the principal frequencies from Fig. 8(a). At the lower 14.3 GHz peak, the radii of the two skyrmions varies massively with this electric field strength of $\langle \Delta r_{\rm Sk_1} \rangle =$ $\langle \Delta r_{\rm Sk_2} \rangle = 13.6 \pm 0.2$ nm. Our hypothesis in Sec. IV C was that to stimulate skyrmion motion, a minimum variation in the skyrmion radius—of 0.44 nm for these micromagnetic energy terms—is required. The variation in radius at the in-phase resonant frequency is clearly large enough to drive motion. Likewise, this also explains the absence of motion at the other resonant breathing mode. The average variation in the radii of the two skyrmions when driven by an electric field at 57.4 GHz are $\langle \Delta r_{\rm Sk_1} \rangle = 0.1768 \pm 0.0001$ nm and $\langle \Delta r_{\rm Sk_2} \rangle =$ 0.1821 ± 0.0001 nm respectively, well below the threshold for motion. This reversal of the frequencies at which motion occurs is a marked difference between the case of driving with an electric field and a magnetic field. We suggest that this arises from the difference in the mechanism of excitation. In the case of the electric field, this is simulated through a change in the anisotropy, which affects the radius of both skyrmions equally. On the other hand, when the breathing modes are excited with a magnetic field, the Zeeman coupling will have an opposite effect on each of the skyrmions due to the antiferromagnetic coupling. Thus, in the magnetic field case, at the in-phase resonant mode, the Zeeman effect will always suppress the oscillation of one of the two skyrmions and so the overall amplitude is smaller. There is no such competition in the electric field/anisotropy case, and so at this resonant mode maximum oscillations are allowed.

VII. SKYRMION MOTION DRIVEN BY PERPENDICULAR CURRENT DENSITIES

In this section, we study the effects of the skyrmion breathing mode excitation by an electric current via a spin-torque mechanism (instead of a microwave magnetic field) in a fully compensated SAF. It has already been shown that a Slonczewski-type spin transfer torque (STT) [56–58] can be used to qualitatively reproduce the effects of the microwave magnetic field when stimulating breathing modes [39]. Here, we extend this to considering the effects of an STT on the

skyrmion velocity in the presence of a static in-plane magnetic field.

To model a Slonczewski type STT, an additional torque term is added to the right-hand side of the LLG [Eq. (1)], given by

$$\vec{\tau}_{SL} = \beta \frac{\epsilon - \alpha \epsilon'}{1 + \alpha^2} [\vec{\mathbf{m}} \times (\vec{\mathbf{m}}_P \times \vec{\mathbf{m}})] - \frac{\epsilon' - \alpha \epsilon}{1 + \alpha^2} (\vec{\mathbf{m}} \times \vec{\mathbf{m}}_P).$$
(11)

Here, $\vec{\mathbf{m}}_P$ is the magnetization of the fixed layer—which is not explicitly simulated—and ϵ and ϵ' represent the effective spin polarization terms for the dampinglike and fieldlike torques, respectively. We can write ϵ as

$$\epsilon = \frac{P\Lambda^2}{(\Lambda^2 + 1) + (\Lambda^2 - 1)(\vec{\mathbf{m}} \cdot \vec{\mathbf{m}}_P)},\tag{12}$$

where P is the spin polarization and the Slonczewski Λ parameter is a dimensionless parameter of the model. Finally, the last dimensionless parameter β is given by

$$\beta = \frac{\hbar J_c}{M_s ed},\tag{13}$$

where J_c is the current density and d is the film thickness. For all subsequent results, we simulate a skyrmion in a system with an antiferromagnetic interlayer exchange coupling energy of $\sigma_{RKKY} = -0.3 \text{ mJ/m}^2$, and driven by a pure dampinglike torque ($\epsilon \neq 0, \epsilon' = 0$). For a Slonczewski-type STT the current density J_c is applied along the out-of-plane axis, in what is described as current perpendicular to plane (CPP). The direction of the fixed layer is also set along the +z direction. A schematic of the simulated system along with the direction of the current density and the polarization of the fixed layer is shown in Fig. 9(a). For all simulations the STT is considered to be present in both ferromagnetic layers. Considering the spin diffusion length l_{Ru} of ruthenium, the material typically chosen as the nonmagnetic spacer layer, of 14 nm [59], this setup is valid [39].

Figure 9(b) shows the spectral response of the system when excited with a sinc pulse of current density of magnitude 1×10^9 A/m². The frequencies of both the in-phase and out-of-phase modes reproduce those shown in Fig. 2(a). As mentioned, the excitation of skyrmion breathing modes with an STT was studied extensively in Ref. [39], where they showed that for their chosen magnetic parameters the breathing modes occurred at the same frequencies regardless of whether they were excited by a magnetic field or a current density. Furthermore, they demonstrated that this was independent of the nature of the STT; demonstrating the same effects with fieldlike STTs ($\epsilon = 0$, $\epsilon' \neq 0$) or a mixture of dampinglike and fieldlike STTs ($\epsilon \neq 0$, $\epsilon' \neq 0$).

Figure 9(c) shows the velocity of the skyrmion as a function of the current density when driven by an oscillating current density with a frequency of 57.6 GHz—which was obtained by fitting to the peak of the out-of-phase breathing mode in Fig. 9(b). The current density was varied in a quasilogarithmic fashion to allow a sampling of a wide range of magnitudes. At current densities much above 5×10^{11} A/m², significant deformation of the skyrmion was

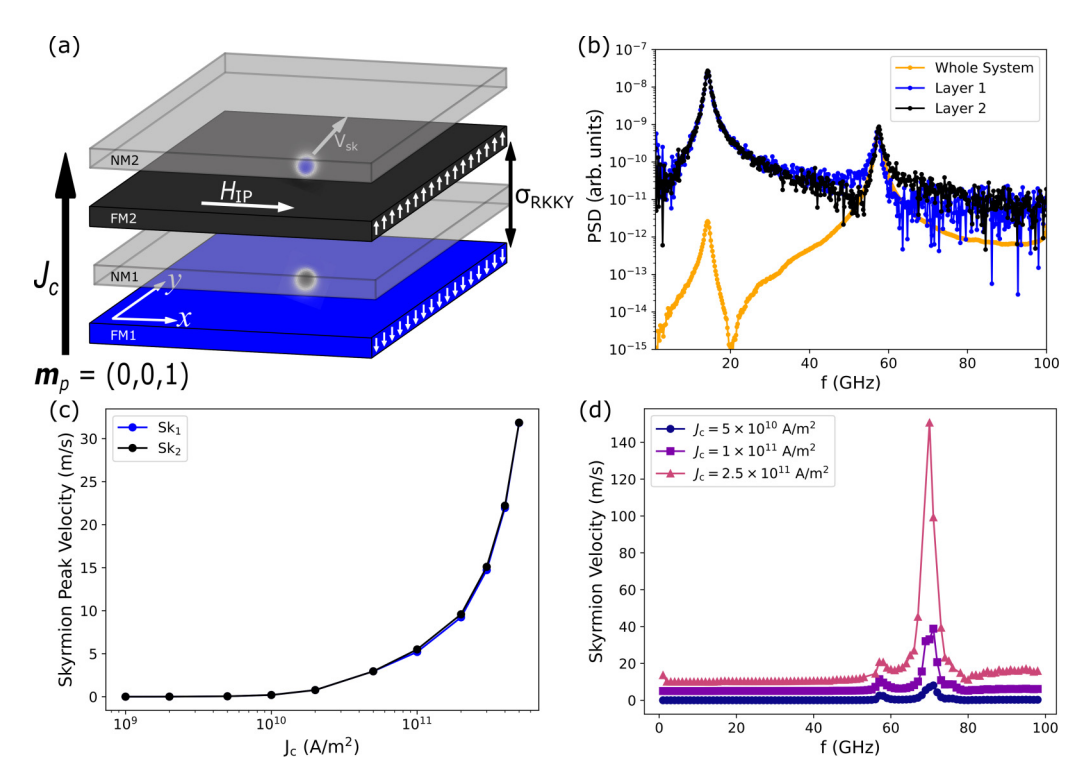


FIG. 9. (a) Illustration of the current perpendicular to plane (CPP) spin transfer torque (STT) geometry, with the direction of the current illustrated with the arrow labeled J_c and the polarization of the fixed layer illustrated with $\mathbf{m_p}$. (b) Spectral response of skyrmion system when stimulated with a CPP-STT with a current density of $1 \times 10^9 \text{A/m}^2$. (c) Skyrmion velocity when driven at the OOP breathing mode resonant frequency of 57.6 GHz found from (b) as a function of current density. (d) Sweeps of the skyrmion velocity as a function of frequency for several representative current densities chosen from (c).

observed, before eventually breaking down at current densities in the 10^{12} A/m² regime (not shown). We extend this to examine the effects of the skyrmion velocity as a function of frequency at current densities of 5×10^{10} , 1×10^{11} , and 2×10^{10} 10^{11} A/m² in Fig. 9(d). The shape of the v(f) is broadly similar to that presented in Fig. 4. However, some important differences should be noted. In a similar way to the magnetic-field driven case, we observe little-to-no evidence of any motion at the resonant frequency of the in-phase breathing mode. This is because the CPP-STT is acting as an effective magnetic field on the skyrmions, and so we expect any behavior to be consistent with the case of driving with a simple magnetic field. The relative velocities of the skyrmions driven at the resonant frequency of the out-of-phase breathing mode and at the resonant frequency of the spin wave mode arising from the canted spins are different. While the absolute magnitude of the velocity depends on the strength of the current density or magnetic field, this relative difference is of note. It arises because a current density along the z axis, with a spin polarization also along the z axis will induce an effective field that acts on the in plane spins. In the case of the skyrmions, this is only the spins in the narrow band around the skyrmion where the magnetization rotates from up to down (and vice-versa for the skyrmion in the other layer). When the spin wave emission is arising from the hybrid skyrmion breathing and resonance of the canted spins of the system, then we would expect this to be coupled much better to the STT, and so increase the velocity of the skyrmion, as we see for each of the current densities in Fig. 9(d).

VIII. CONCLUSION

To conclude, we have used micromagnetic simulations to demonstrate a new method for stimulating skyrmion motion in a synthetic antiferromagnet using only global magnetic fields. We have used a microwave frequency out-of-plane magnetic field to excite skyrmion breathing, which in the presence of a static in-plane field emits spin waves asymmetrically. Through characterization of the breathing modes of the skyrmions in our systems we have understood the underlying relationship between skyrmion velocity and the frequency of the driving field, observing that the maximum skyrmion velocity occurs at the characteristic frequency of the out-of-phase skyrmion breathing mode.

We have further measured the variation in radius of the skyrmions at different driving fields to understand that there is a threshold magnitude of radius variation, only above which will skyrmion motion be driven.

The understanding of the coupling between the skyrmion velocity and the out-of-phase breathing mode has allowed us to properly understand the relationship between the velocity and the antiferromagnetic interlayer exchange coupling strength, where we define three different regimes of skyrmion motion depending on the magnitude of the antiferromagnetic exchange coupling.

We have also extended our study to consider synthetic ferrimagnets, which is relevant to experimental studies where a perfect compensation of moments is difficult to achieve. We show that as expected, the velocity is at a maximum when the system is fully compensated, however motion is possible over a wide range of decompensation, and this is true for low and relatively high coupling strength (in comparison to what has been reported experimentally).

Finally, we have compared our results to the cases when driven by a microwave electric field and oscillating current densities. By doing this, we have revealed both the true origin of the relationship between velocity and exchange coupling, and the reason for the lower frequency of skyrmion motion when driven by electric fields compared to magnetic fields, as well as demonstrating the wide range of mechanisms through which this spin wave emission skyrmion motion can be driven. These results will help to inform the design of future novel

computing architectures based on the dynamics of skyrmions in synthetic antiferromagnets.

ACKNOWLEDGMENTS

This project was funded by the UK Government Department for Science, Innovation and Technology through National Measurement System funding (Metrology of complex systems for low energy computation). The project was also supported by EPSRC Grant No. EP/T006803/1.

DATA AVAILABILITY

The data that support the findings of this article are openly available [60].

- [1] N. Nagaosa and Y. Tokura, Topological properties and dynamics of magnetic skyrmions, Nat. Nanotechnol. **8**, 899 (2013).
- [2] K. Everschor-Sitte, J. Masell, R. M. Reeve, and M. Kläui, Perspective: Magnetic skyrmions—overview of recent progress in an active research field, J. Appl. Phys. 124, 240901 (2018).
- [3] C. H. Marrows and K. Zeissler, Perspective on skyrmion spintronics, Appl. Phys. Lett. **119**, 250502 (2021).
- [4] G. Finocchio, F. Büttner, R. Tomasello, M. Carpentieri, and M. Kläui, Magnetic skyrmions: from fundamental to applications, J. Phys. D 49, 423001 (2016).
- [5] R. Tomasello, E. Martinez, R. Zivieri, L. Torres, M. Carpentieri, and G. Finocchio, A strategy for the design of skyrmion racetrack memories, Sci. Rep. 4, 6784 (2014).
- [6] K. M. Song, J.-S. Jeong, B. Pan, X. Zhang, J. Xia, S. Cha, T.-E. Park, K. Kim, S. Finizio, J. Raabe, J. Chang, Y. Zhou, W. Zhao, W. Kang, H. Ju, and S. Woo, Skyrmion-based artificial synapses for neuromorphic computing, Nat. Electron. 3, 148 (2020).
- [7] C. H. Marrows, J. Barker, T. A. Moore, and T. Moorsom, Neuromorphic computing with spintronics, npj Spintronics 2, 12 (2024).
- [8] A. P. Petrović, C. Psaroudaki, P. Fischer, M. Garst, and C. Panagopoulos, Colloquium: Quantum properties and functionalities of magnetic skyrmions, Rev. Mod. Phys. 97, 031001 (2025).
- [9] N. Banerjee, C. Bell, C. Ciccarelli, T. Hesjedal, F. Johnson, H. Kurebayashi, T. A. Moore, C. Moutafis, H. L. Stern, I. J. Vera-Marun, J. Wade, C. Barton, M. R. Connolly, N. J. Curson, K. Fallon, A. J. Fisher, D. A. Gangloff, W. Griggs, E. Linfield, C. H. Marrows *et al.*, Materials for quantum technologies: a roadmap for spin and topology, arXiv:2406.07720
- [10] A. Fert, V. Cros, and J. Sampaio, Skyrmions on the track, Nat. Nanotechnol. 8, 152 (2013).
- [11] S. Woo, K. Litzius, B. Krüger, M.-Y. Im, L. Caretta, K. Richter, M. Mann, A. Krone, R. M. Reeve, M. Weigand, P. Agrawal, I. Lemesh, M.-A. Mawass, P. Fischer, M. Kläui, and G. S. D. Beach, Observation of room-temperature magnetic skyrmions and their current-driven dynamics in ultrathin metallic ferromagnets, Nat. Mater. 15, 501 (2016).
- [12] R. Juge, S.-G. Je, D. S. Chaves, L. D. Buda-Prejbeanu, J. Peña Garcia, J. Nath, I. M. Miron, K. G. Rana, L. Aballe, M. Foerster, F. Genuzio, T. O. Mentes, A. Locatelli, F. Maccherozzi, S. S. Dhesi, M. Belmeguenai, Y. Roussigné, S. Auffret, S. Pizzini,

- G. Gaudin *et al.*, Current-driven skyrmion dynamics and drivedependent skyrmion Hall effect in an ultrathin film, Phys. Rev. Appl. 12, 044007 (2019).
- [13] S. L. Zhang, W. W. Wang, D. M. Burn, H. Peng, H. Berger, A. Bauer, C. Pfleiderer, G. van der Laan, and T. Hesjedal, Manipulation of skyrmion motion by magnetic field gradients, Nat. Commun. 9, 2115 (2018).
- [14] C. Wang, D. Xiao, X. Chen, Y. Zhou, and Y. Liu, Manipulating and trapping skyrmions by magnetic field gradients, New J. Phys. 19, 083008 (2017).
- [15] K.-W. Moon, D.-H. Kim, S.-G. Je, B. S. Chun, W. Kim, Z. Q. Qiu, S.-B. Choe, and C. Hwang, Skyrmion motion driven by oscillating magnetic field, Sci. Rep. 6, 20360 (2016).
- [16] W. Wang, M. Beg, B. Zhang, W. Kuch, and H. Fangohr, Driving magnetic skyrmions with microwave fields, Phys. Rev. B 92, 020403(R) (2015).
- [17] K. Everschor-Sitte and M. Sitte, Real-space berry phases: Skyrmion soccer (invited), J. Appl. Phys. 115, 172602 (2014).
- [18] W. Jiang, X. Zhang, G. Yu, W. Zhang, X. Wang, M. Benjamin Jungfleisch, J. Pearson, X. Cheng, O. Heinonen, K. L. Wang, Y. Zhou, A. Hoffmann, and S. te Velthuis, Direct observation of the skyrmion Hall effect, Nat. Phys. 13, 162 (2017).
- [19] K. Litzius, I. Lemesh, B. Krüger, P. Bassirian, L. Caretta, K. Richter, F. Büttner, K. Sato, O. A. Tretiakov, J. Förster, R. M. Reeve, M. Weigand, I. Bykova, H. Stoll, G. Schütz, G. S. D. Beach, and M. Kläui, Skyrmion Hall effect revealed by direct time-resolved x-ray microscopy, Nat. Phys. 13, 170 (2017).
- [20] K. Zeissler, S. Finizio, C. Barton, A. J. Huxtable, J. Massey, J. Raabe, A. V. Sadovnikov, S. A. Nikitov, R. Brearton, T. Hesjedal, G. van der Laan, M. C. Rosamond, E. H. Linfield, G. Burnell, and C. H. Marrows, Diameter-independent skyrmion Hall angle observed in chiral magnetic multilayers, Nat. Commun. 11, 428 (2020).
- [21] X. Zhang, Y. Zhou, and M. Ezawa, Magnetic bilayer-skyrmions without skyrmion Hall effect, Nat. Commun. 7, 10293 (2016).
- [22] R. A. Duine, K.-J. Lee, S. S. P. Parkin, and M. D. Stiles, Synthetic antiferromagnetic spintronics, Nat. Phys. 14, 217 (2018).
- [23] J. Barker and O. A. Tretiakov, Static and dynamical properties of antiferromagnetic skyrmions in the presence of applied current and temperature, Phys. Rev. Lett. 116, 147203 (2016).
- [24] F. Büttner, I. Lemesh, and G. S. D. Beach, Theory of isolated magnetic skyrmions: From fundamentals to room temperature applications, Sci. Rep. 8, 4464 (2018).

- [25] W. Legrand, D. Maccariello, F. Ajejas, S. Collin, A. Vecchiola, K. Bouzehouane, N. Reyren, V. Cros, and A. Fert, Roomtemperature stabilization of antiferromagnetic skyrmions in synthetic antiferromagnets, Nat. Mater. 19, 34 (2020).
- [26] R. Juge, N. Sisodia, J. U. Larrañaga, Q. Zhang, V. T. Pham, K. G. Rana, B. Sarpi, N. Mille, S. Stanescu, R. Belkhou, M.-A. Mawass, N. Novakovic-Marinkovic, F. Kronast, M. Weigand, J. Gräfe, S. Wintz, S. Finizio, J. Raabe, L. Aballe, M. Foerster et al., Skyrmions in synthetic antiferromagnets and their nucleation via electrical current and ultra-fast laser illumination, Nat. Commun. 13, 4807 (2022).
- [27] V. T. Pham, N. Sisodia, I. D. Manici, J. Urrestarazu-Larrañaga, K. Bairagi, J. Pelloux-Prayer, R. Guedas, L. D. Buda-Prejbeanu, S. Auffret, A. Locatelli, T. O. Menteş, S. Pizzini, P. Kumar, A. Finco, V. Jacques, G. Gaudin, and O. Boulle, Fast current-induced skyrmion motion in synthetic antiferromagnets, Science 384, 307 (2024).
- [28] S.-H. Yang, K.-S. Ryu, and S. Parkin, Domain-wall velocities of up to 750 ms⁻¹ driven by exchange coupling torque in synthetic antiferromagnets, Nat. Nanotechnol. 10, 221 (2015).
- [29] S. Lepadatu, H. Saarikoski, R. Beacham, M. J. Benitez, T. A. Moore, G. Burnell, S. Sugimoto, D. Yesudas, M. C. Wheeler, J. Miguel, S. S. Dhesi, D. McGrouther, S. McVitie, G. Tatara, and C. H. Marrows, Synthetic ferrimagnet nanowires with very low critical current density for coupled domain wall motion, Sci. Rep. 7, 1640 (2017).
- [30] C. E. A. Barker, S. Finizio, E. Haltz, S. Mayr, P. M. Shepley, T. A. Moore, G. Burnell, J. Raabe, and C. H. Marrows, Domain wall motion at low current density in a synthetic antiferromagnet nanowire, J. Phys. D 56, 425002 (2023).
- [31] K. Wang, V. Bheemarasetty, and G. Xiao, Spin textures in synthetic antiferromagnets: Challenges, opportunities, and future directions, APL Mater. 11, 070902 (2023).
- [32] T. Dohi, S. DuttaGupta, S. Fukami, and H. Ohno, Formation and current-induced motion of synthetic antiferromagnetic skyrmion bubbles, Nat. Commun. 10, 5153 (2019).
- [33] M. Lonsky and A. Hoffmann, Dynamic excitations of chiral magnetic textures, APL Mater. 8, 100903 (2020).
- [34] M. Mochizuki, Spin-wave modes and their intense excitation effects in skyrmion crystals, Phys. Rev. Lett. **108**, 017601 (2012).
- [35] Y. Onose, Y. Okamura, S. Seki, S. Ishiwata, and Y. Tokura, Observation of magnetic excitations of skyrmion crystal in a helimagnetic insulator Cu₂OSeO₃, Phys. Rev. Lett. 109, 037603 (2012).
- [36] J.-V. Kim, F. Garcia-Sanchez, J. Sampaio, C. Moreau-Luchaire, V. Cros, and A. Fert, Breathing modes of confined skyrmions in ultrathin magnetic dots, Phys. Rev. B 90, 064410 (2014).
- [37] B. Satywali, V. P. Kravchuk, L. Pan, M. Raju, S. He, F. Ma, A. P. Petrović, M. Garst, and C. Panagopoulos, Microwave resonances of magnetic skyrmions in thin film multilayers, Nat. Commun. 12, 1909 (2021).
- [38] T. Srivastava, Y. Sassi, F. Ajejas, A. Vecchiola, I. Ngouagnia Yemeli, H. Hurdequint, K. Bouzehouane, N. Reyren, V. Cros, T. Devolder, J.-V. Kim, and G. de Loubens, Resonant dynamics of three-dimensional skyrmionic textures in thin film multilayers, APL Mater. 11, 061110 (2023).
- [39] M. Lonsky and A. Hoffmann, Coupled skyrmion breathing modes in synthetic ferri- and antiferromagnets, Phys. Rev. B 102, 104403 (2020).

- [40] C. E. A. Barker, E. Haltz, T. A. Moore, and C. H. Marrows, Breathing modes of skyrmion strings in a synthetic antiferromagnet multilayer, J. Appl. Phys. 133, 113901 (2023).
- [41] L. Xing, D. Hua, and W. Wang, Magnetic excitations of skyrmions in antiferromagnetic-exchange coupled disks, J. Appl. Phys. 124, 123904 (2018).
- [42] J. Chen, J. Hu, and H. Yu, Chiral emission of exchange spin waves by magnetic skyrmions, ACS Nano 15, 4372 (2021).
- [43] S. A. Díaz, T. Hirosawa, D. Loss, and C. Psaroudaki, Spin wave radiation by a topological charge dipole, Nano Lett. 20, 6556 (2020).
- [44] N. Tang, W. L. N. C. Liyanage, S. A. Montoya, S. Patel, L. J. Quigley, A. J. Grutter, M. R. Fitzsimmons, S. Sinha, J. A. Borchers, E. E. Fullerton, L. DeBeer-Schmitt, and D. A. Gilbert, Skyrmion-excited spin wave fractal networks, Adv. Mater. 35, 2300416 (2023).
- [45] H. Y. Yuan, X. S. Wang, M.-H. Yung, and X. R. Wang, Wiggling skyrmion propagation under parametric pumping, Phys. Rev. B **99**, 014428 (2019).
- [46] C. Liu, F. Ai, S. Reisbick, A. Zong, A. Pofelski, M.-G. Han, F. Camino, C. Jing, V. Lomakin, and Y. Zhu, Correlated spinwave generation and domain-wall oscillation in a topologically textured magnetic film, Nat. Mater. 24, 406 (2025).
- [47] L. Qiu, L. Shen, X. Zhang, Y. Zhou, G. Zhao, W. Xia, H.-B. Luo, and J. P. Liu, Interlayer coupling effect on skyrmion dynamics in synthetic antiferromagnets, Appl. Phys. Lett. 118, 082403 (2021).
- [48] B. Göbel, I. Mertig, and O. A. Tretiakov, Beyond skyrmions: Review and perspectives of alternative magnetic quasiparticles, Phys. Rep. **895**, 1 (2021).
- [49] D. Girardi, S. Finizio, C. Donnelly, G. Rubini, S. Mayr, V. Levati, S. Cuccurullo, F. Maspero, J. Raabe, D. Petti, and E. Albisetti, Three-dimensional spin wave dynamics, localization and interference in a synthetic antiferromagnet, Nat. Commun. 15, 3057 (2024).
- [50] A. Vansteenkiste, J. Leliaert, M. Dvornik, M. Helsen, F. Garcia-Sanchez, and B. Van Waeyenberge, The design and verification of MuMax3, AIP Adv. 4, 107133 (2014).
- [51] W. Jiang, G. Chen, K. Liu, J. Zang, S. G. te Velthuis, and A. Hoffmann, Skyrmions in magnetic multilayers, Phys. Rep. 704, 1 (2017).
- [52] See Supplemental Material at http://link.aps.org/supplemental/ 10.1103/j6y9-dj7f for the simulated hysteresis loops of the system; an explanation of the resonance mode arising from the canted spins; a description of the supplementary videos; an explanation of the calculation of the time-varying skyrmion radius; and further data supporting Fig. 7 of the main paper for an antiferromagnetic interlayer exchange coupling strength of -0.3 mJ/m².
- [53] C. E. A. Barker, K. Fallon, C. Barton, E. Haltz, T. P. Almeida, S. Villa, C. Kirkbride, F. Maccherozzi, B. Sarpi, S. S. Dhesi, D. McGrouther, S. McVitie, T. A. Moore, O. Kazakova, and C. H. Marrows, Phase coexistence and transitions between antiferromagnetic and ferromagnetic states in a synthetic antiferromagnet, Phys. Rev. B 109, 134437 (2024).
- [54] E. Haltz, C. E. A. Barker, and C. H. Marrows, Statics and dynamics of skyrmions in balanced and unbalanced synthetic antiferromagnets, arXiv:2309.03697.

- [55] P. K. Mishra, M. Sravani, A. Bose, and S. Bhuktare, Voltage-controlled magnetic anisotropy-based spintronic devices for magnetic memory applications: Challenges and perspectives, J. Appl. Phys. 135, 220701 (2024).
- [56] J. Slonczewski, Current-driven excitation of magnetic multilayers, J. Magn. Magn. Mater. 159, L1 (1996).
- [57] L. Berger, Emission of spin waves by a magnetic multilayer traversed by a current, Phys. Rev. B **54**, 9353 (1996).
- [58] J. Xiao, A. Zangwill, and M. D. Stiles, Boltzmann test of Slonczewski's theory of spin-transfer torque, Phys. Rev. B 70, 172405 (2004).
- [59] K. Eid, R. Fonck, M. A. Darwish, W. P. Pratt, Jr., and J. Bass, Current-perpendicular-to-plane-magnetoresistance properties of Ru and Co/Ru interfaces, J. Appl. Phys. **91**, 8102 (2002).
- [60] C. E. A. Barker, C. Parton-Barr, C. H. Marrows, O. Kazakova, and C. Barton, Research Data Leeds, https://doi.org/10.5518/ 1742 (2025).